Formation window of gas bubble superlattice in molybdenum under ion implantation

Cheng Sun,[1,*] David J. Sprouster,[2,3] Yongfeng Zhang,[1,4] Di Chen,[5] Yongqiang Wang,[5] Lynne E. Ecker,[2] and Jian Gan[1]

[1]*Idaho National Laboratory, Idaho Falls, Idaho 83415, USA*

[2]*Brookhaven National Laboratory, Upton, New York 11973, USA*

[3]*Department of Materials Science and Chemical Engineering, Stony Brook University, Stony Brook, New York 11794, USA*

[4]*Department of Engineering Physics, University of Wisconsin-Madison, Madison, Wisconsin 53706, USA*

[5]*Los Alamos National Laboratory, Los Alamos, New Mexico 87545, USA*

(Received 10 June 2019; published 31 October 2019)

Self-assembly of defects in materials can create novel physical properties with potential applications in various technological fields. Here, we studied the physical mechanism of self-assembly of helium gas bubbles in molybdenum under ion implantation and unified the formation window of gas bubble/void superlattice in terms of irradiation temperatures and helium-atomic parts per million/displacements per atom damage levels. The ion fluence and temperature-dependent formation of gas bubble superlattice in molybdenum was examined via both transmission electron microscopy and synchrotron-based small-angle x-ray scattering. The formation of gas bubble superlattice is linked with specific implantation conditions, including ion fluence and implantation temperature. The bubble lattice constant increases with increasing the implantation temperature from 150 to 450 °C. Once the gas bubble superlattice forms, increasing fluence has no effect on the bubble lattice constant. Both experiments and atomic kinetic Monte Carlo modeling indicate a three-stage formation process of gas bubble superlattice, from random bubbles to planar ordering and then to three-dimensional superlattices, suggesting that one-dimensional diffusion of self-interstitial atoms can cause the formation of gas bubble superlattice. Our study advances the understanding of defect self-assembly in materials in nonequilibrium states and provides an approach of managing the defect formation and transforming them from a liability into an asset in a controllable way.

DOI: 10.1103/PhysRevMaterials.3.103607

I. INTRODUCTION

Under injection with energetic particles, self-assembly of defects in materials occurs and leads to the formation of ordered defect structures, such as void lattice, gas bubble lattice, stacking fault tetrahedron alignments, etc. [1–3]. The ordering of the defects in materials can create novel physical properties with potential applications in various fields. Shinada *et al.* [4]. demonstrated the enhanced semiconductor device performance using ordered dopant arrays induced by single-ion implantation. The fluctuations of the turn-on voltage of the semiconductor transistors with ordered dopant arrays are less than those structures with conventional random doping. Low-energy Ar^+ ion implantation has been used to produce self-organized quantum dots on GaSb surfaces with potential optoelectronic and photovoltaic applications [5]. Klehe *et al.* [6]. reported that the pressure-induced oxygen-defect ordering can result in the increase of the superconducting transition temperature in Tl_2Ba_2CuO due to the transfer of hole carriers to or from the CuO_2 plane. Liu *et al.* [7]. used helium ion implantation to fabricate porous rutile TiO_2 nanorod array photoelectrodes, which exhibit ten times higher photocurrent density than nonimplanted TiO_2 nanorod array, and the introduced helium bubbles can trap holes inside to separate the charge carriers and therefore were considered as the main contributor to the enhancement of photocurrent density.

The formation of gas bubble superlattices has been reported in a variety of metals [2,8–13], such as body-centered cubic (bcc) Mo, face-centered cubic (fcc) Cu, and hexagonally close-packed Ti. Planar ordering, where the bubbles order only on specific planes, and three-dimensional ordering, where the bubbles form a superlattice, were reported in the literature. Johnson and Mazey [14] performed pioneering ion-implantation studies with 30–50 keV He^+ into several bcc metals, including V, W, Mo, Cr, Fe, and Ta, and demonstrated that gas bubble superlattice forms at implantation temperatures of $\sim 0.2T_m$ (T_m is the melting temperature). Lawson and Johnson [15]. reported a lower temperature threshold ($0.14–0.16T_m$) for bubble superlattice formation in Mo under He ion implantation, and suggested that vacancy mobility has a critical influence on the development of gas bubble superlattice. Ion-implantation induced gas bubble development in Cu was directly observed by *in situ* irradiation experiments in a transmission electron microscope (TEM) [16], in which the gas bubbles first nucleated in a disordered arrangement and subsequently evolved into an ordered state under further irradiation. Wang *et al.* [17] revealed the mechanical response of He-implanted Cu hosting a gas bubble superlattice. The He bubble superlattices in Cu became disordered when plasticly deformed and exhibited a twinninglike transformation as a result of lattice shearing through twinning partial dislocation. The self-organization of gas bubbles typically adopts the

*cheng.sun@inl.gov; chengsun2008@gmail.com

same structure as the host matrix crystal structure [18]. In contrast, Gan *et al.* [19,20]. recently reported that fission gas Xe bubbles form a fcc superlattice in bcc U-Mo after neutron irradiation at around 373 K to a fission density of 4.5×10^{21} fissions/cm^3.

Some possible theories of self-assembly of gas bubbles in metals have been proposed in the literature [1,21–25]. Yu and Lu [21] developed a phase-field model that contains both elasticity and diffusion-interaction process and concluded that phase separation and anisotropic diffusion mainly contribute to the self-assembly of nanovoids and nanobubbles under irradiation. Dubinko *et al.* [22] proposed a dislocation interaction mechanism based on dislocation loop punching from growing bubbles. The ordering of gas bubbles is considered as the result of dislocation repulsion and diffusion attraction between bubbles that operate simultaneously. A concept of low-dimensional diffusion of self-interstitial atoms was also proposed for the gas bubble lattice formation [3]. Hu *et al.* [26]. integrated a first-passage Monte Carlo method into a phase-field model to study the gas bubble superlattice in the irradiated U-Mo metallic fuels. The simulation indicates that fast one-dimensional (1D) migration of interstitials along ⟨110⟩ directions is attributed to the gas bubble alignment along ⟨110⟩ orientations in the bcc-structured U-Mo host materials and implies that the formation of fcc-structured gas bubble superlattice is due to the fast migration of U interstitials along ⟨110⟩ directions. Recently, Gao *et al.* [24]. has proposed a rate theory-based framework for void superlattice formation. It is shown that the superlattice resulted from an instability in the vacancy concentration field. The nanoscale superlattice parameter is stabilized by the competition between phase-separation kinetics and defect dynamics, and the superlattice structure is dictated by anisotropic self-interstitial-atom (SIA) diffusion. The model can be extended to explain gas bubble superlattice formation in W with the consideration of gas atom trapping of vacancy diffusion [27]. In addition, preexisting defects in the solids can tune the alignment of gas bubbles by serving as sinks for point defects under irradiation. Molecular statics calculation reveals that the segregation of vacancies and helium atoms towards the screw dislocation results in the formation of He bubble superlattice at nodes of screw dislocations [28].

Gas bubble superlattice has been extensively studied in various metals in the literature; the physical mechanism and formation window are still not clear. In this work, He gas ion-implantation experiments are carried out to establish the formation window of He gas bubble superlattices, and it is shown that gas bubble and void superlattice may be unified using the parameter gas parts per million/displacements per atom (appm/dpa) ratio, which is zero for void superlattices and can vary for gas bubble superlattices. The dependences of gas bubble size and bubble lattice constant on irradiation condition are investigated in the light of void superlattices. The same trends are obtained on the effects of temperature, ion flux, and fluences for both void and gas bubble superlattices. The experimental observations are supported by simulations, which show that, similar to void superlattices, gas bubble superlattice formation can also be caused by anisotropic SIA diffusion. Our study advances the fundamental understanding of the defect self-assembly in irradiated materials and provides insights on managing the defect formation to tailor desired microstructure under implantation.

II. MATERIALS AND METHODOLOGIES

A. Helium ion implantation

Mo sheets with purity of 99.95 wt% was purchased from Goodfellow. He ion implantations were performed in the Ion Beam Materials Laboratory at Los Alamos National Laboratory. He ions at energies of 40 keV were implanted in perforated Mo TEM samples at temperatures of 150, 300, and 450 °C with ion fluences from 3×10^{16} to 2×10^{17} He/cm^2 at a constant flux of 7.6×10^{12} He/cm^2/s ($\sim 1 \times 10^{-4}$ dpa/s). The stopping and range of ions in matter (SRIM) code [29] was used to predict the profile of He ion concentration, damage levels, and the ratio of He-appm over the number of displacement per atom (dpa) in Mo. The Kinchin-Pease method was used in the calculation with a Mo displacement energy of 60 eV. As seen in Fig. S1 [30], with 40-keV He implantation, the peak damage occurs at depth of ∼100 nm, while the peak He concentration is located at depth of ∼130 nm. With ion fluence of 2×10^{17} He/cm^2, the peak dose in the region of interest is ∼4 dpa.

B. Microstructure characterization via TEM and small-angle x-ray scattering

The microstructure of He ion implanted Mo was characterized using both TEM and synchrotron-based small-angle x-ray scattering (SAXS). A Tecnai-F30 (300-keV) TEM equipped with Gatan charge-coupled device camera was used to examine the perforated Mo TEM samples, prepared by twin-jet electropolishing in a 12.5% sulfuric acid and 87.5% methanol solution at a temperature of ∼5 °C. Transmission SAXS measurements were performed at the Life Science X-ray Scattering (LIX) beamline at the National Synchrotron Light Source-II [31], using 15.50-keV x rays with a wavelength of 0.7998 Å. Two-dimensional maps of the scattering intensity were collected over a 200×200-μm^2 area with a 2-μm x-ray beam spot. The scattering intensity was collected on the samples with a detector distance of 3861.86 mm. The scattering pattern from unimplanted samples was subtracted from all He implanted samples to isolate the signal from the Mo host lattice and gas bubble superlattice. The individual SAXS detector images were reduced in the IGOR-Pro based software package NIKA [32]. He bubble size distributions were determined by fitting the scattering intensity using the nonlinear least-squares method in IRENA [33]. For a polydisperse spherical scattering system and electron density (ρ), embedded in a medium with electron density (ρ_0), the scattering intensity $I(Q)$ is given by

$$I(Q) = V^2 \times (\Delta\rho)^2 \times F(Q) \times S(Q), \quad (1)$$

where V is the volume of the scattering particles, $(\Delta\rho)^2$ is the square of the difference in electron density between the particle and the background media ($\Delta\rho = \rho - \rho_0$) and $F(Q)$ is the form/shape factor and $S(Q)$ is the interparticle interaction parameter [34]. A Gaussian size distribution was used to model the bubble size distribution and an interprecipitate structure factor to account for the high bubble densities and

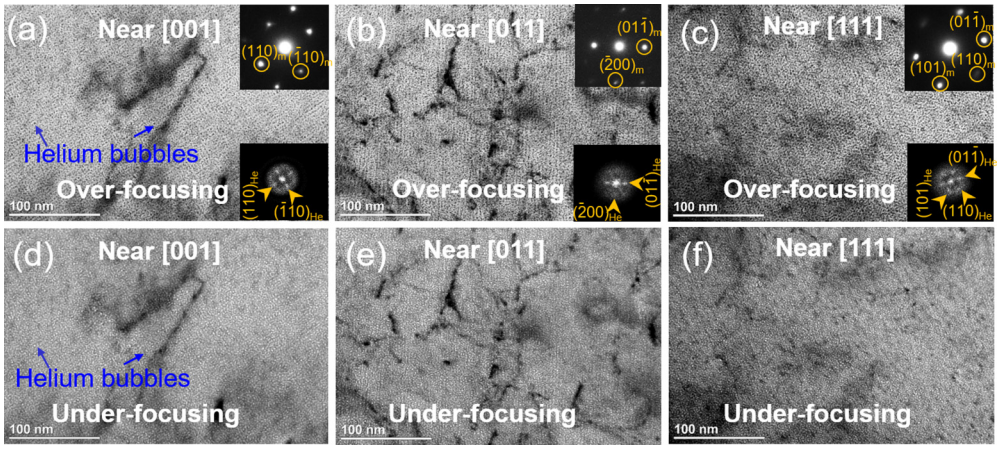

FIG. 1. Bright-field TEM micrographs of gas bubbles assembly in Mo implanted with He ions at 300 °C to a fluence of 2×10^{17} He/cm^2 along the zone axis close to [001], [011], and [111]. He bubbles exhibit as dark contrast under overfocusing imaging condition (a)–(c) and bright contrast under underfocusing imaging condition (d)–(f). The selected area diffraction and fast Fourier transfer pattern were superimposed in the TEM micrographs. The structure of He gas bubble superlattice is isomorphic with the Mo host matrix.

additional scattering intensity in the samples with gas bubble superlattice.

C. Modeling method

Atomic kinetic Monte Carlo (AKMC) simulations were carried out to show how 1D SIA diffusion affect gas bubble superlattice formation and the effects of temperature, fluence, and flux. Due to the very low migration barrier of SIAs (∼0.05 eV), SIAs diffuse very fast even at very low temperatures, limiting the total physical time that can be simulated. Therefore, it is not feasible to use the same dose rates as used in the experiments. As shown in Ref. [24], there is a positive correlation between temperature and dose rate for superlattice formation. Accordingly, higher temperatures were needed in the AKMC simulations for gas bubble superlattice (GBS) formation when higher dose rates were used. The intension here is not to make quantitative comparison on gas bubble size and GBS parameter with experiments, but to study the formation characters of gas bubble superlattices to elucidate the role of 1D SIA diffusion. Here, we adopted the AKMC method used in Gao *et al.* [24]., which was developed for void superlattice formation, to describe vacancy (V) and interstitial (SIA) production and evolution. Similar to that for void superlattices, 1D SIA diffusion along ⟨111⟩ directions is adopted in the simulations. A mean-field sink, represented by mean-free jumps of vacancy and SIA [24], is used for preexisting sinks such as dislocations. To describe He, the octahedral sublattice of a bcc crystal was included, as shown in Fig. S2 [30]. Following Deo *et al.* [35], a He atom can either occupy an octahedral site as an interstitial (He_{int}), or a bcc site as a substitution (He_{sub}). Note that they were denoted as different types of atoms in the AKMC method. Similar to the Mo/V/SIA system [24], pairwise bonds within the second-nearest-neighbor cutoff were used to describe the interaction between He atoms, and that between a He atom and a vacancy or a Mo atom. The interaction between a He atom and an SIA was not considered in the current model. The bond energies were fitted to energetics of He and He/V clusters in bcc Mo from density-function theory calculations. The data used in the fitting include the formation energies of He interstitial (5.28 eV), He substitution (4.64 eV), HeV_2 cluster (6.81 eV), He_2V cluster (7.25 eV), and He_2V_2 (8.15 eV) cluster in bcc Mo [36], and the binding energy between two He_{int} (0.97 eV) [37]. It is further assumed that a pure bcc/octahedral He phase is of zero cohesive energy. All pairwise bond energies are summarized in Table S1 [30]. For all simulations, the simulated cell is periodic with a dimension of 80 by 80 by 80 a_0^3, with a_0 being the lattice parameter of bcc Mo. More details regarding the modeling method are described in the Supplemental Material [30].

III. RESULTS

Figure 1 shows the bright-field TEM micrographs of He bubbles in Mo implanted at 300 °C to a dose of 2×10^{17} He/cm^2. He gas bubbles exhibit dark contrast as the TEM micrographs were taken with an overfocusing imaging condition in Figs. 1(a)–1(c) and bright contrast with an underfocusing imaging condition in Figs. 1(d)–1(f). He gas bubble self-assembly was shown in a zone axis close to [001], [011], and [111]. The selected area diffraction (SAD) pattern and fast Fourier transformation (FFT) pattern were superimposed on the TEM micrographs. The spots in FFT patterns indicate the structural arrangement of He gas bubbles exhibits superlattice structure. The comparison between SAD and FFT patterns with zone axis close to [001], [011], and [111] confirms that the structural arrangement of He gas bubbles is isomorphic with the host bcc-structured Mo lattice.

The fluence- and temperature-dependent self-assembly of He gas bubbles in Mo were studied with TEM and SAXS. The bright-field TEM micrographs were taken with the zone axis close to [001], [011], and [111], as shown in Fig. 2, Fig. S3, and Fig. S4 [30], respectively. The evolution of He gas bubbles under He implantation at 300 °C to a fluence from 3×10^{16} to 1×10^{17} He/cm^2 was shown in Figs. 2(a)–2(c). At a fluence of 3×10^{16} He/cm^2, He gas bubbles with average diameter (d_{bubble}) of ∼0.9 nm were randomly formed within the matrix. See Table I. As the fluence increases to

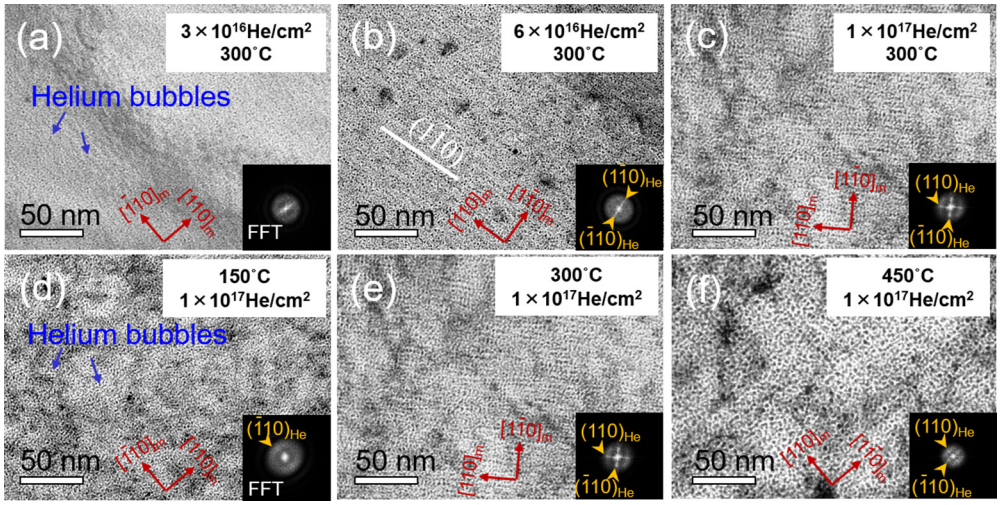

FIG. 2. Bright-field TEM micrographs of gas bubbles assembly in Mo under He implantation at various implantation conditions. Over-focusing imaging conditions, with zone axis close to [001] were used to visualize He gas bubbles. The fast Fourier transformation pattern was superimposed in the micrographs to show the evidence of gas bubble superlattice. (a)–(c) The arrangement of He gas bubbles in Mo after implantation at 300 ˚C to a fluence from 3×10^{16} to 1×10^{17} He/cm^2. The assembly of He bubble commences at fluence of 6×10^{16} He/cm^2; the bubbles order initially on {011} planes as manifested by the inset FFT pattern. (d)–(f) The arrangements of He gas bubbles after implantation to a fluence of 1×10^{17} He/cm^2 at temperatures from 150 to 450 °C.

6×10^{16} He/cm^2, d_{bubble} increases to ∼1.2 nm and both bright-field TEM micrograph and the inset FFT pattern reveal the gas bubbles self-organize preferentially on {011} planes. At fluences up to 1×10^{17} He/cm^2, 3D ordering of gas bubbles occurs in Mo as manifested by bright-field TEM micrographs and corresponding FFT patterns at zone axis of [001], [011] and [111] in Fig. 2, Fig. S3, and Fig. S4 [30]. The gas bubble lattice constant (a_{bubble}) was calculated to be 5.0 nm via analysis of the inverse FFT patterns using

$$a_{hkl} = d_{hkl}\sqrt{h^2 + k^2 + l^2}, \tag{2}$$

where d_{hkl} is the d spacing along [h k l] orientation. The development of gas bubble superlattice at implantation temperatures from 150 to 450 °C is shown in Figs. 2(d)–2(f). At a temperature of 150 °C, the gas bubbles with average diameter of ∼1.0 nm exhibit ordering on $(\bar{1}10)$ plane in some regions and the FFT patterns shows weak spots on $(\bar{1}10)$ $(\bar{1}10)$ plane. At 300 °C, the formation of a gas bubble superlattice was observed as manifested as spots in the FFT patterns and d_{bubble} increases to 1.4 nm. As the implantation temperature increases to 450 °C, the gas bubble superlattice still forms and d_{bubble} further increases to ∼2.2 nm. The a_{bubble} increases from ∼3.8 to ∼7.6 nm as the implantation temperature increases from 150 to 450 °C. The evolution of He gas bubbles under zone axis close to [011] and [111] showed the same dependence on ion fluence and temperature, as revealed in Fig. S3 and Fig. S4 [30].

SAXS measurement of gas bubble assembly in Mo is shown in Fig. 3. Figures 3(a)–3(d) show the two-dimensional (2D) SAXS patterns at fluence from 3×10^{16} to 2×10^{17} He/cm^2 at 300 °C. He gas bubble superlattices were observed at fluences of 1×10^{17} He/cm^2 and 2×10^{17} He/cm^2, as evidenced by diffraction peaks observed in the 2D SAXS patterns. Figures 3(e)–3(g) show the 2D SAXS patterns after implantation to 1×10^{17} He/cm^2 at temperatures from 150–450 °C. Well-defined gas bubble superlattice peaks in the SAXS patterns were observed after implantation at 300 and 450 ˚C. The integrated SAXS patterns of all the above implantation conditions were shown in Fig. 4. Samples implanted to a fluence of 1×10^{17} and 2×10^{17} He/cm^2 at 300 °C and implanted at a temperature of 300 and 450 °C to a fluence of

TABLE I. Helium ion implantation conditions and measurements via TEM and SAXS.

Energy (keV)	Fluence (ions/cm^2)	Temperature (°C)	d_{bubble}[a] (nm)		a_{bubble}[b] (nm)	
			TEM	SAXS	TEM	SAXS
40	3.0×10^{16}	300	0.9 ± 0.2	1.0 ± 0.4		
40	6.0×10^{16}	300	1.2 ± 0.2	1.1 ± 0.4	5.2 ± 0.1	5.1 ± 0.8
40	1.0×10^{17}	300	1.4 ± 0.2	1.3 ± 0.5	5.0 ± 0.2	5.2 ± 0.3
40	2.0×10^{17}	300	1.4 ± 0.2	1.6 ± 0.5	5.1 ± 0.2	5.2 ± 0.3
40	1.0×10^{17}	150	1.1 ± 0.2	1.2 ± 0.4	3.8 ± 0.2	3.2 ± 0.7
40	1.0×10^{17}	450	2.2 ± 0.3	2.7 ± 0.5	7.6 ± 0.4	7.1 ± 0.5

[a]d_{bubble} is the diameter of the gas bubbles.
[b]a_{bubble} is the gas bubble lattice constant.

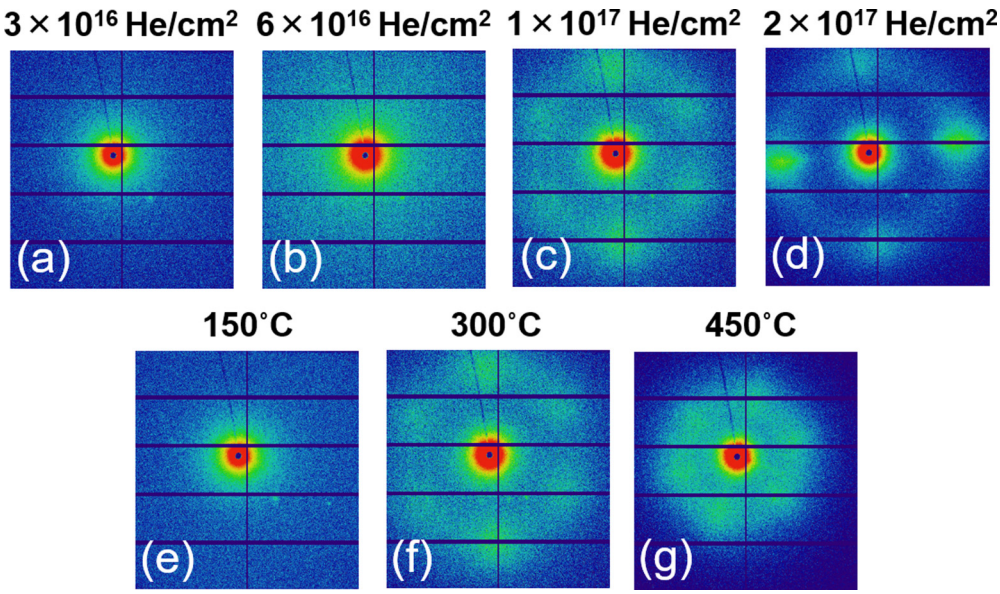

FIG. 3. SAXS measurement of gas bubble assembly in Mo after implantation at various conditions. (a)–(d) Two-dimensional SAXS patterns of implanted molybdenum after exposure from 3×10^{16} to 2×10^{17} He/cm^2 (0.6-4 dpa) at 300 °C. (e)–(g) Two-dimensional SAXS patterns of Mo after implantation to 1×10^{17} He/cm^2 at temperature from 150 to 450 °C.

1×10^{17} He/cm^2 show diffraction peaks, indicating the formation of gas bubble superlattice, consistent with the observations from TEM described above. In Fig. 4(a), the peak magnitudes increase with ion fluence with no change in scattering vector, suggesting the independence of a_{bubble} with increasing ion fluence. In Fig. 4(b), scattering vector decreases with temperature, indicating that a_{bubble} increases with temperature. Interestingly, the sample implanted at 300 °C exhibits the largest magnitude of diffraction peak compared to the samples implanted at 150 and 450 °C. Figure 5 shows the evolution of a_{bubble} and d_{bubble} for these implantation conditions. The measurements from TEM and SAXS are plotted in Fig. 5 for comparison. Both TEM and SAXS measurements reveal that a_{bubble} is insensitive to ion fluence, while d_{bubble} increases and then saturates with increasing ion fluence up to 2×10^{17} He/cm^2 at 300 °C. Implanting with the same ion fluence of 1×10^{17} He/cm^2, both a_{bubble} and d_{bubble} increase with increasing implantation temperature from 150 to 450 °C.

Figure 6 presents the schematics of ion fluence and temperature-dependent He gas bubbles distribution in Mo with zone axis of [001]. The arrangement of He gas bubbles evolves from random arrays, 2D ordering on {110} planes to 3D gas bubble superlattice with increasing ion fluence, as seen in the upper row in Fig. 6. d_{bubble} increases with ion fluence, while a_{bubble} is observed to be independent of ion fluence. The gas bubble superlattice forms within a specific temperature range, below which He gas bubbles are randomly distributed and above which the gas bubble superlattice starts to disorder, as seen in the lower row in Fig. 6. a_{bubble} increases with implantation temperature.

IV. DISCUSSION

A. Formation window of gas bubble and void superlattice

The window of gas bubble and void superlattice may be unified using the parameter gas appm/dpa ratio, which

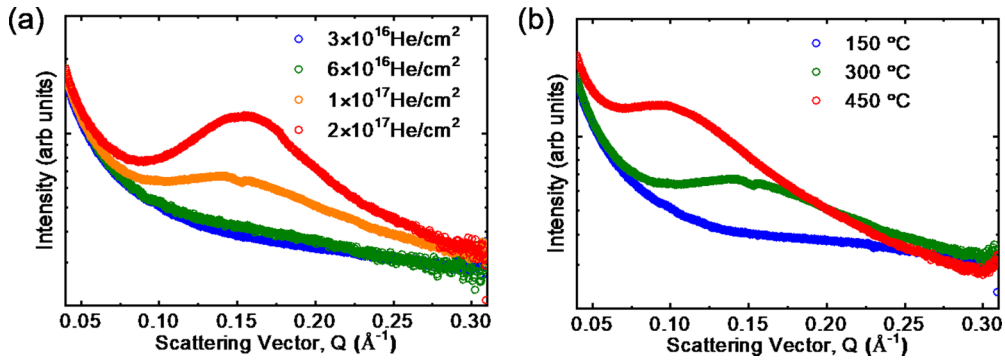

FIG. 4. (a) Plot of intensity vs scattering vector of gas bubbles in Mo irradiated to an ion fluence from 3×10^{16} to 2×10^{17} He/cm^2 (0.6–4 dpa) at 300 °C. (b) Plot of intensity vs scattering vector with a fixed fluence of 1×10^{17} He/cm^2 at temperatures from 150 to 450 °C.

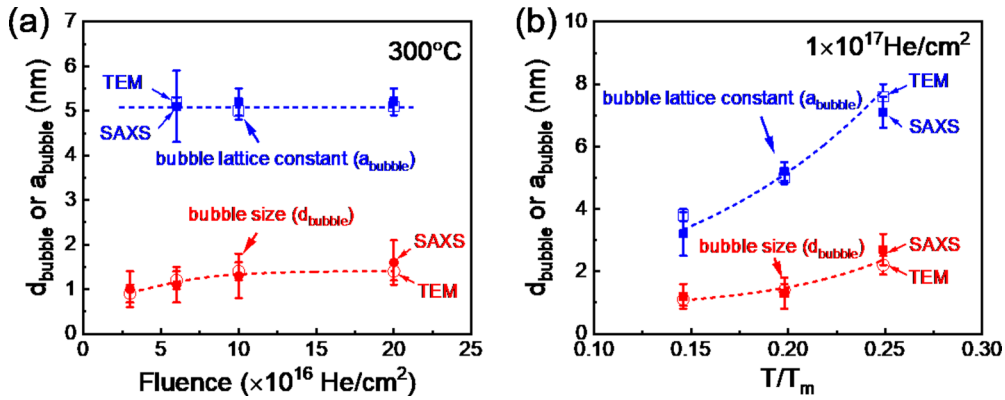

FIG. 5. Measurement of bubble lattice constant and bubble size using both TEM and SAXS (with dashed lines as a guide to the eye). (a) Plot of bubble lattice constant and bubble size as a function of ion fluence at 300 °C. The bubble lattice constant is insensitive to the ion fluence, while the bubble size initially increases with ion fluence and then saturates at fluence of 1×10^{17} He/cm^2. (b) Plot of bubble lattice constant and bubble size as a function of implantation temperature (T/T_m) at 1×10^{17} He/cm^2. Both bubble lattice constant and bubble size increase with implantation temperature.

is zero for void superlattices and can vary for gas bubble superlattices. In Fig. 7, the formation window of He gas bubble and void superlattice in Mo was constructed in terms of He appm/dpa and implantation temperature (T_m/T, where T_m is the melting point). The solid symbols and open symbols represent the ordered void/bubble lattice and random voids/bubbles, respectively [15,38–42]. The cited values of He appm/dpa were calculated using SRIM based on the implantation conditions reported in the literature. The ordering of gas bubbles and voids occurs only at specific implantation/irradiation temperature range and He appm/dpa damage conditions, as seen in the formation window in Fig. 7. A lower bound and an upper bound in temperature, as shown by the curves, can be established. Similar to void ordering [24,43], the lower-temperature bound of gas bubble superlattice marks the recombination limit, below which small bubbles are not stable against recombination flux. As will be shown below from simulations, with increasing temperature, the role of recombination becomes less significant. Because the ordering of bubbles (or voids) is caused by recombination of vacancies with SIAs which diffuse anisotropically, bubble ordering weakens as the temperature increases. This leads to an upper-temperature bound, above which bubbles are stable but not ordered to form a superlattice. We note that although a solid line is used to help visualization, the transition from superlattice to disordered bubbles upon adjusting temperature or He appm/dpa should be gradual. It is also seen from Fig. 7 that as He appm/dpa increases, the lower-temperature bound decreases, meaning that He bubble superlattice can form at lower temperatures with higher He appm/dpa than void superlattices do. For the high-solution energy of He atoms, with

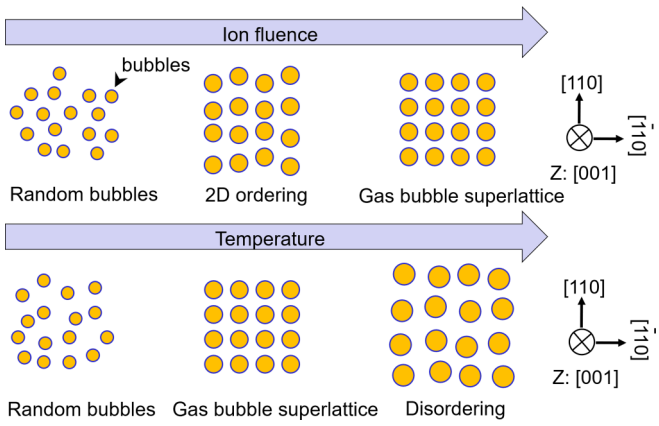

FIG. 6. Schematics of gas bubble self-assembly in Mo under He ion implantation with zone axis of [001]. The arrangement of helium gas bubbles evolves from random arrays, 2D ordering on {110} planes to 3D gas bubble superlattice with increasing ion fluence (upper row). The gas bubble lattice constant is observed to be independent of ion fluence. Gas bubble superlattice only forms within a specific temperature range and disordering occurs at higher temperature (lower row).

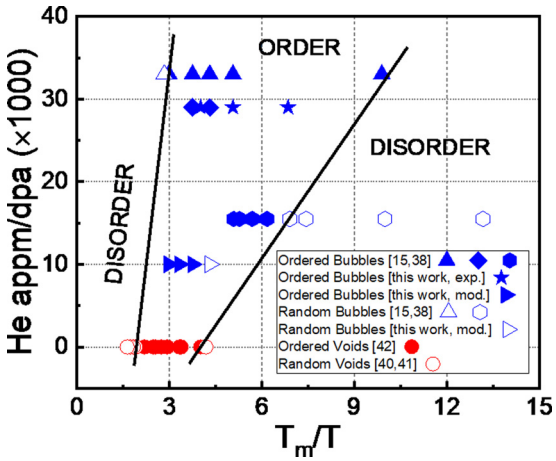

FIG. 7. Formation window of ordered gas bubble lattice and void lattice in Mo in terms of He appm/dpa and implantation/irradiation temperature (T_m/T). The ordering of gas bubbles and voids occurs only at specific implantation/irradiation conditions. The formation of void lattice requires higher temperature range and increasing the value of He appm/dpa lowers the implantation temperature required for gas bubble superlattice formation.

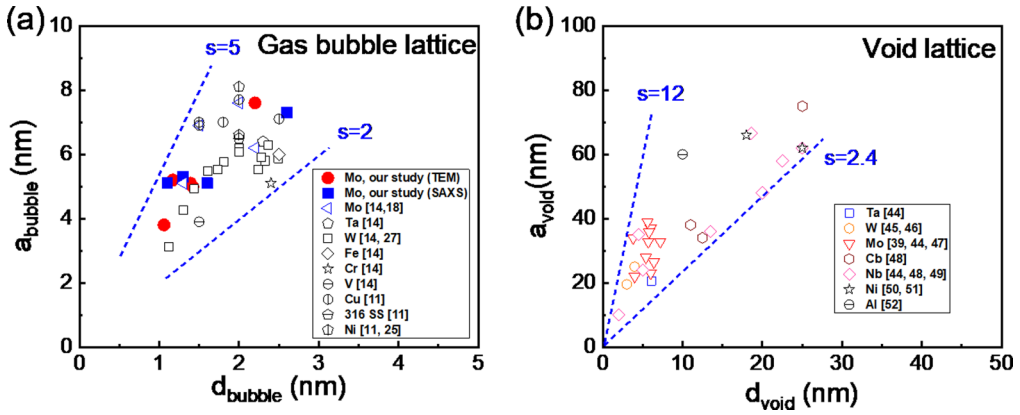

FIG. 8. (a) Gas bubble lattice constant (a_{bubble}) as a function of gas bubble diameter (d_{bubble}) for various metals with gas bubble superlattice implanted at various conditions. The ratio (s) of a_{bubble} to d_{bubble} falls between 2 and 5. (b) Plot of void lattice constant (a_{void}) versus void diameter (d_{void}) for various metals with void lattice. The ratio (s) of a_{void} to d_{void} is in the range between 2.4 and 12.

the same bubble size, a higher He/V ratio will make bubbles more stable against recombination. Effectively, this will move the lower-temperature bound, which is caused by the recombination limit, towards lower temperatures as the He appm/dpa value increases. The fact that void superlattices and gas bubble lattices can be included in the same formation window in Fig. 7 indicates their similarity of formation mechanisms. It is natural to expect a gradual transition from void superlattices to gas bubble lattices as the He appm/dpa ratio increases from zero for the former to finite values for the latter, because inert gases have strong tendencies of occupying voids. As will be discussed later, the similarity of their formation mechanisms is also suggested by AKMC simulations.

The gas bubble lattice constant (a_{bubble}) was plotted as a function of gas bubble diameter (d_{bubble}) for various metals with He gas bubble superlattice implanted at various conditions in Fig. 8. Both our results (solid dots) and the literature data (open dots) were plotted in Fig. 8(a). The ratio of a_{bubble} to d_{bubble} (s) falls between 2 and 5, independent of the implantation conditions. Such ratio for void lattice is around 2.4–12 [39,44–52], as shown in Fig. 8(b). The difference is attributed to the relatively higher irradiation temperature and dpa damage required for void lattice formation.

B. Formation mechanism of gas bubble and void superlattice

The mechanism of forming gas bubble superlattice was studied by AKMC modeling and compared to that of void superlattice. AKMC simulations with 1D SIA diffusion along ⟨111⟩ were performed in bcc Mo to investigate the role of 1D SIA diffusion in gas bubble superlattice formation and the effect of temperature and fluence. Four temperatures, 400, 500, 600, and 700 °C, were used in the simulations, and the dose rate was set to be 0.98 dpa/s with a gas to dpa ratio of 0.01 (i.e., He appm/dpa rate of 10 000). The simulations were run up to 98 dpa. At 500 to 700 °C, formation of GBSs was observed to start at dose levels of several dpa (see Fig. 9), comparable to that in the experiments. At the lowest temperature simulated (400 °C), no superlattice formation has been seen at a dose of 98 dpa. As mentioned in Sec. II C, the higher temperatures and dose rates than those in experiments were used for the efficiency of AKMC simulations. The purpose here is not to make quantitative comparison with experiments, but to study the formation characters of gas bubble superlattices and compare with void superlattice. GBSs (ordered bubbles) were observed to nucleate when an instability in the vacancy concentration field occurred. The wavelength developed at the instability, as shown by the radial distribution function of vacancies and He substitutes in Fig. 9(e), defined the average interbubble distance and eventually the GBS lattice constant. This wavelength did not change once it was formed in the simulations. Same as for void superlattices [24], the 1D SIA diffusion along ⟨111⟩ led to the formation of a bcc-structured He GBS.

Several excellent agreements with experimental observations are noticed. First, a three-stage formation process, from random bubbles to {110} planar ordering and then a 3D superlattice, is observed in both experiments and simulations. Such a three-stage process is clear in Figs. 9(a)–9(d) showing the snapshots of He gas bubble evolution in Mo at 600 °C to a dose of 0.98, 2.9, 10.8, and 58.8 dpa, projected along [100] orientation. Second, the bubble lattice constant, once developed, is independent of fluence, while the ordering keeps improving upon increasing fluence. To show that, the radial distribution function of He atoms, which is the averaged volumetric density of He atoms as a function of distance from a He atom, is calculated at four different doses. As shown in in Fig. 9(e), once a wavelength in He concentration (i.e., the interplane distance of close-packed-planes, {110} here) develops, it is kept constant upon increasing dose. This indicates that the bubble lattice constant, once developed, is independent of fluences, consistent with experiments. The height of the peaks increases due to improved ordering over increasing dose. Meanwhile, the first peak moves towards the right, indicating further growth of individual gas bubbles. Third, it is observed from the simulations that the formation of superlattice strongly depends on temperature. The simulated GBS formation conditions in terms of the He appm/dpa ratio and temperature are within the experimentally established formation window, as shown in Fig. 7. Note that the temperature bound could be different from that observed in the experiments due to the much higher dose rate used. A higher

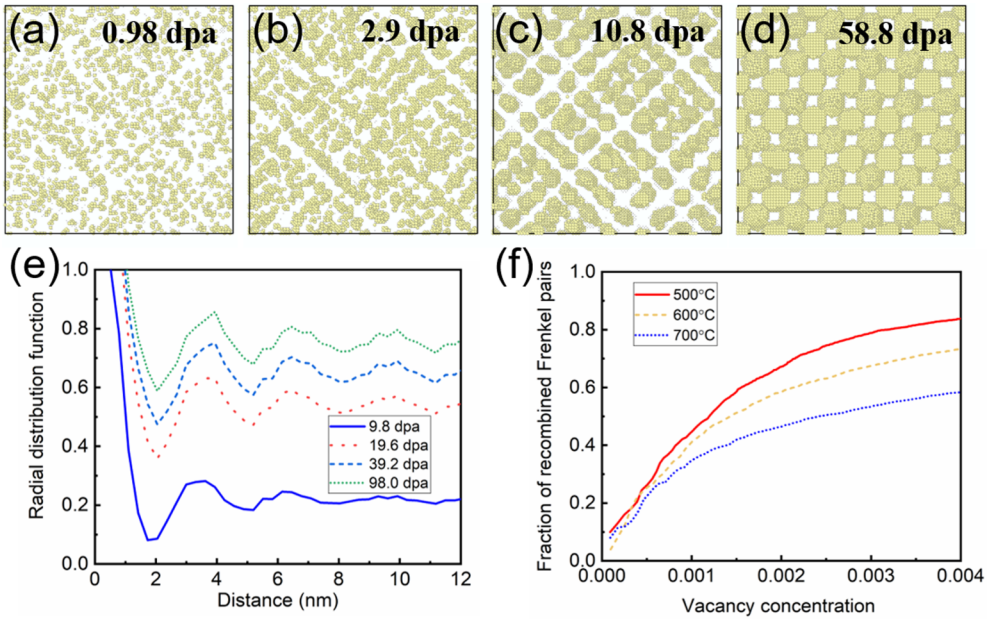

FIG. 9. Atomic kinetic Monte Carlo simulation on the self-assembly of gas bubbles in Mo under He ion bombardment. The dimension of the simulated cell is $80 \times 80 \times 80\ a_0^3$ (a_0 is the lattice parameter of bcc Mo). Snapshots showing the arrangement of He gas bubbles at (a) 0.98, (b) 2.9, (c) 10.8, and (d) 58.8 dpa at 600 °C are projected along [100] direction. Large atoms represent He substitutions and small dots represent unoccupied vacancies. The gas bubbles evolve from a random distribution to planar ordering and then a 3D superlattice. (e) Radial distribution function of vacancies and gas substitutes showing the development of wavelength at different damage levels up to 98 dpa. (f) Fraction of recombined Frenkel pairs relative to the total production at 500, 600, and 700 °C.

temperature is needed for superlattice formation with a higher dose rate [24]. Superlattice formation is observed in simulations at 500, 600, and 700 °C, but the ordering weakens with increasing temperature. When temperature increases, sink absorption of vacancies becomes more important. As such, the fraction of point defects that are annihilated by recombination decreases, as shown in Fig. 9(f). Because the ordering of bubbles is caused by recombination of vacancies with SIAs which diffuse one dimensionally, weaker ordering is seen at higher temperature. Such temperature effect on the gas bubble ordering was also observed in our experiments, as seen in Fig. 4. The bubble lattice constant also increases from 3.2 to 3.6 nm and then to 4.2 nm with the simulation temperature increase from 500 to 600 °C and then to 700 °C. These agreements between simulations and experiments suggest that 1D SIA diffusion is likely the mechanism that causes the gas bubble superlattice formation, similar to void superlattice formation.

V. CONCLUSIONS

We studied the self-assembly of gas bubbles in molybdenum under He ion implantation and constructed the formation window of gas bubble and void superlattice in terms of irradiation temperatures and He appm/dpa damage conditions. The formation of gas bubble superlattice is linked with specific value of gas appm/dpa and temperatures. The bubble lattice constant shows negligible dependence on the ion fluence, while it increases with implantation temperature. Our experimental and AKMC studies suggest that 1D diffusion of SIAs can cause the formation of gas bubble superlattice. A three-stage formation process, from random bubbles to planar ordering and then to 3D superlattices, is seen from both AKMC simulations and He-ion irradiation experiments. Our experimental and modeling study provides fundamental mechanisms on the gas bubble superlattice in metals and advances the understanding of defects self-assembly in materials in non-equilibrium states.

ACKNOWLEDGMENTS

This work was sponsored by the US Department of Energy (DOE), Office of Science, Basic Energy & Science, Materials Sciences and Engineering Division under FWP No. C000-14-003 at Idaho National Laboratory operated by Battelle Energy Alliance under Contract No. DE-AC07-05ID14517. We also acknowledge the US DOE, Office of Nuclear Energy Nuclear Science User Facility under Contract No. DE-AC07-051D14517 and Office of Sciences User Facility Center for Integrated Nanotechnologies at Los Alamos National Laboratory under Contract No. DE-AC52-06NA25396. This research used the LIX beamline at the National Synchrotron Light Source-II, a DOE, Office of Science User Facility operated for the DOE, Office of Science by Brookhaven National Laboratory under Contract No. DESC0012704. The LiX beamline is part of the Life Science Biomedical Technology Research resource, primarily supported by the National Institute of Health, National Institute of General Medical Sciences under Grant No. P41 GM111244, and by the DOE Office of Biological and Environmental Research under Grant No. KP1605010, with additional support from NIH Grant No. S10 OD012331.

[1] K. Krishan, Kinetics of void-lattice formation in metals, Nature (London) **287**, 420 (1980).

[2] P. B. Johnson, A. L. Malcolm, and D. J. Mazey, Importance of stress in bubble ordering in the helium gas-bubble superlattice in copper, Nature (London) **329**, 316 (1987).

[3] W. Jäger and H. Trinkaus, Defect ordering in metals under irradiation, J. Nucl. Mater. **205**, 394 (1993).

[4] T. Shinada *et al.*, Enhancing semiconductor device performance using ordered dopant arrays, Nature (London) **437**, 1128 (2005).

[5] S. Facsko *et al.*, Formation of ordered nanoscale semiconductor dots by ion sputtering, Science **285**, 1551 (1999).

[6] A. K. Klehe *et al.*, Pressure-induced oxygen ordering phenomena in high-Tc superconductors, Physica C **257**, 105 (1996).

[7] Y. Liu *et al.*, Fabrication of porous TiO_2 nanorod array photoelectrodes with enhanced photoelectrochemical water splitting by helium ion implantation, Nanoscale **8**, 10642 (2016).

[8] P. B. Johnson and D. J. Mazey, Helium gas-bubble superlattice in copper and nickel, Nature (London) **281**, 359 (1979).

[9] R. W. Harrison *et al.*, Engineering self-organising helium bubble lattices in tungsten, Sci. Rep. **7**, 7724 (2017).

[10] P. B. Johnson and D. J. Mazey, Helium gas bubble lattices in face-centred-cubic metals, Nature (London) **276**, 595 (1978).

[11] P. B. Johnson and D. J. Mazey, The gas-bubble superlattice and the development of surface structure in He^+ and H irradiated metals at 300 K, J. Nucl. Mater. **93–94**, 721 (1980).

[12] P. B. Johnson, K. L. Reader, and R. W. Thomson, Transverse sections from helium-implanted copper using ultramicrotomy, J. Nucl. Mater. **231**, 92 (1996).

[13] A. R. Totemeier, Helium ion implantation in zirconium: Bubble formation and growth, Doctoral dissertation, Texas A & M University, Texas, 2015.

[14] P. B. Johnson and D. J. Mazey, Gas-bubble superlattice formation in bcc metals, J. Nucl. Mater. **218**, 273 (1995).

[15] F. E. Lawson and P. B. Johnson, A temperature threshold for gas-bubble superlattice formation in molybdenum, J. Nucl. Mater. **252**, 34 (1998).

[16] S. E. Donnelly *et al.*, *In-situ* TEM studies of ion-irradiation induced bubble development and mechanical deformation in model nuclear materials, Mater. Res. Soc. Proc, **1645**, mrsf13-1645-ee10-01 (2014).

[17] Z.-J. Wang *et al.*, Mechanical behavior of copper containing a gas-bubble superlattice, Acta Mater. **121**, 78 (2016).

[18] P. B. Johnson and F. Lawson, Helium gas-bubble superlattice formation in molybdenum, Nucl. Instrum. Methods Phys. Res. Sect. B **243**, 325 (2006).

[19] J. Gan *et al.*, Transmission electron microscopy characterization of irradiated U–7Mo/Al–2Si dispersion fuel, J. Nucl. Mater. **396**, 234 (2010).

[20] J. Gan *et al.*, Thermal stability of fission gas bubble superlattice in irradiated U–10Mo fuel, J. Nucl. Mater. **464**, 1 (2015).

[21] H.-C. Yu and W. Lu, Dynamics of the self-assembly of nanovoids and nanobubbles in solids, Acta Mater. **53**, 1799 (2005).

[22] V. I. Dubinko *et al.*, The theory of gas bubble lattice, Radiat. Eff. **100**, 85 (1986).

[23] J. R. Willis, The interaction of gas bubbles in an anisotropic elastic solid, J. Mech. Phys. Solids **23**, 129 (1975).

[24] Y. Gao *et al.*, Theoretical prediction and atomic kinetic Monte Carlo simulations of void superlattice self-organization under irradiation, Sci. Rep. **8**, 6629 (2018).

[25] W. Jäger and J. Roth, Microstructure of Ni and stainless steel after multiple energy He and D implantation, J. Nucl. Mater. **93–94**, 756 (1980).

[26] S. Hu *et al.*, Formation mechanism of gas bubble superlattice in UMo metal fuels: Phase-field modeling investigation, J. Nucl. Mater. **479**, 202 (2016).

[27] D. J. Sprouster *et al.*, Irradiation-dependent helium gas bubble superlattice in tungsten, Sci. Rep. **9**, 2277 (2019).

[28] Z. Di, X.-M. Bai, Q. Wei, J. Won, R. G. Hoagland, Y. Wang, A. Misra, B. P. Uberuaga, and M. Nastasi, Tunable helium bubble superlattice ordered by screw dislocation network, Phys. Rev. B **84**, 052101 (2011).

[29] J. F. Ziegler, M. D. Ziegler, and J. P. Biersack, SRIM – The stopping and range of ions in matter, Nucl. Instrum. Methods Phys. Res. Sect. B **268**, 1818 (2010).

[30] See Supplemental Material at http://link.aps.org/supplemental/10.1103/PhysRevMaterials.3.103607 for supporting figures and additional description of modeling method.

[31] J. DiFabio, S. Chodankar, S. Pjerov, J. Jakoncic, M. Lucas, C. Krywka, V. Graziano, and L. Yang, The life science x-ray scattering beamline at NSLS-II, in *Proceedings of the 12th International Conference on Synchrotron Radiation Instrumentation - SRI2015*, edited by Q. Shen and C. Nelson, AIP COnf. Proc. No. 1741 (AIP, New York, 2016), p. 030049.

[32] J. Ilavsky, Nika: Software for two-dimensional data reduction, J. Appl. Crystallogr. **45**, 324 (2012).

[33] J. Ilavsky and P. Jemian, Irena: Tool suite for modeling and analysis of small-angle scattering, J. Appl. Crystallogr. **42**, 347 (2009).

[34] E.-W. Huang *et al.*, Study of nanoprecipitates in a nickel-based superalloy using small-angle neutron scattering and transmission electron microscopy, Appl. Phys. Lett. **93**, 161904 (2008).

[35] C. S. Deo *et al.*, Helium bubble nucleation in bcc iron studied by kinetic Monte Carlo simulations, J. Nucl. Mater. **361**, 141 (2007).

[36] O. Runevall and N. Sandberg, Helium cluster dissolution in molybdenum, J. Phys.: Condens. Matter **21**, 335401 (2009).

[37] P. Zhang, T. Zou, and J. Zhao, He–He and He–metal interactions in transition metals from first-principles, J. Nucl. Mater. **467**, 465 (2015).

[38] D. J. Mazey *et al.*, A transmission electron microscopy study of molybdenum irradiated with helium ions, J. Nucl. Mater. **64**, 145 (1977).

[39] J. H. Evans, Void swelling and irradiation-induced void shrinkage in neutron irradiated molybdenum and TZM, J. Nucl. Mater. **88**, 31 (1980).

[40] J. F. Stubbins, J. Moteff, and A. Taylor, Void swelling behavior of vanadium ion irradiated molybdenum, J. Nucl. Mater. **101**, 64 (1981).

[41] F. A. Garner and J. F. Stubbins, Saturation of swelling in neutron-irradiated molybdenum and its dependence on irradiation temperature and starting microstructural state, J. Nucl. Mater. **212–215**, 1298 (1994).

[42] J. L. Brimhall and E P. Simonen, Microstructure of Ion Bombarded Single Crystal Molybdenum, in *Conference on Defects and Defect Clusters in BCC Metals and Their Alloys, Gaithersburg, MD* (US Department of Energy, 1973).

[43] N. M. Ghoniem, D. Walgraef, and S. J. Zinkle, Theory and experiment of nanostructure self-organization in irradiated materials, J. Comput. Aided Mater. Des. **8**, 1 (2001).

[44] F. W. Wiffen, The effects of alloying and purity on the formation and ordering of voids in bcc metals, in *Proceedings of International Conference on Radiation-Induced Voids in Metals*, Albany, NY (US Department of Energy, 1972).

[45] J. Moteff, V. K. Sikka, and H. Jang, *The Physics of Irradiation Produced Voids*, edited by R. S. Nelson (AERE Harwell, Oxfordshire, 1975), pp. 181–187.

[46] V. K. Sikka and J. Moteff, Superlattice of voids in neutron-irradiated tungsten, J. Appl. Phys., **43**4942 (1972).

[47] J. H. Evans, Observations of a regular void array in high purity molybdenum irradiated with 2 MeV nitrogen ions, Nature (London) **229**, 403 (1971).

[48] G. L. Kulcinski and J. L. Brimhall, Ordered defect structures in irradiated metals, Technical Report No. BNWL-SA-4047; CONF-710917-3, US Department of Energy, United States, 1971, doi: 10.2172/4556953.

[49] B. A. Loomis, S. B. Gerber, and A. Taylor, Void ordering in ion-irradiated Nb and Nb-1% Zr, J. Nucl. Mater. **68**, 19 (1977).

[50] G. L. Kulcinski, J. L. Brimhall, and H. E. Kissinger, Production of voids in pure metals by high-energy heavy ion bombardment, Technical Report No. BNWL-SA-3966; CONF-710601-8, US Department of Energy, United States, 1971, doi:10.2172/4722246.

[51] G. L. Kulcinski, J. L. Brimhall, and H. E. Kissinger, Production of voids in nickel with high energy selenium ions, J. Nucl. Mater. **40**, 166 (1971).

[52] D. J. Mazey, S. Francis, and J. A. Hudson, Observation of a partially-ordered void lattice in aluminium irradiated with 400 keV Al^+ ions, J. Nucl. Mater. **47**, 137 (1973).